A Novel Radiometric Cross-Calibration of GF-6/WFV With MODIS at the Dunhuang Radiometric Calibration Site

Jie Han, Zui Tao, Yong Xie, Huina Li, Qiyue Liu, and Xiaoguo Guan

***Abstract*—To obtain more abundant target information for vegetation remote sensing research, the wide field of view (WFV) of the GaoFen-6 (GF-6) satellite utilizes eight bands, including four new bands. Unfortunately, it finds the unavailable reference bands from well-calibrated sensors to implement radiometric cross-calibration of the WFV sensor for these new bands, which severely affects the radiometric quality estimation and the radiometric degradation detection of WFV. Therefore, taking the Dunhuang radiometric calibration site (DRCS) in China as the radiometric transfer platform and treating the moderate-resolution imaging spectroradiometer as a reference sensor, a novel radiometric cross-calibration method for WFV is proposed. The validation results show that compared with the official calibration coefficients (OCCs) published by the China centre for resources satellite data and application (CRESDA), the proposed method can obtain reliable radiometric cross-calibration results for each band even without available corresponding reference bands. Moreover, the influences of the interpolation method and the spectral band adjustment factor (SBAF) correction on the calibration results are discussed. The total radiometric cross-calibration uncertainty is less than 4.33%.**

***Index Terms*—GaoFen-6 (GF-6), moderate-resolution imaging spectroradiometer (MODIS), cross-calibration, validation and evaluation.**

I Introduction

ON-ORBIT radiometric calibration is essential for quantitative remote sensing applications of satellite images, which can accurately convert the digital number (DN) of satellite images to the top of atmosphere (TOA) reflectance or the at-sensor radiance [1]. Due to external environmental changes and the radiometric degradation of sensors, this article should be implemented regularly and in a timely manner [2].

For sensors without an onboard calibration assembly, the selection of an appropriate reference sensor with a high radiometric quality and a similar band setting as the calibrated sensor and a cross-calibration method with a low cost, high calibration frequency and recalibration for historical images has been widely used to obtain on-orbit radiometric calibration coefficients for each band [3]. For instance, taking Landsat-8/OLI (operational land imager), moderate-resolution imaging spectroradiometer (MODIS) and Sentinel-2/MSI (multispectral instrument) as the radiometric references, Gao *et al.* applied the cross-calibration method to GF-4/VNIR [visible and near-infrared (NIR)] at the DRCS, Dalate site and Baotou site, and estimated the degradation of GF-4/VNIR [4]. Yang *et al*. evaluated the radiometric capability of GF-6/WFV by using Landsat-8/OLI image and DEM (digital elevation model) established with ZY-3/TLC (three-line camera) to develop the bidirectional reflectance distribution function (BRDF) of the Badain Jaran Desert site and implemented the cross-calibration of GF-6/WFV with the support of MOD05 and time-series MODIS data and validated the cross-calibration results using synchronized ground measurements at the DRCS [5]. Gao *et al*. carried out a radiometric cross-calibration of FY-3C (feng yun-3C)/VIRR (visible infrared radiometer) based on the Suomi-NPP (suomi national polar-orbiting partnership)/VIIRS (visible infrared imaging radiometer suite) at the DRCS [6]. Li *et al.* developed an improved cross-calibration method to recalibrate GF-1/WFV with Landsat-8/OLI data as a reference [7]. Xie *et al*. introduced the radiometric block adjustment algorithm into the cross-calibration of the GF-1/WFV sensor, achieved a high absolute radiometric calibration accuracy and reduced the relative radiometric difference between adjacent WFV cameras [8]. Feng *et al*. proposed a novel radiometric cross-calibration method to solve large view angle-associated problems when using Landsat-8/OLI data to calibrate GF-1/WFV. The total uncertainty of this cross-calibration method is ∼8% [9]. Liu *et al*. used valid MODIS images of sunny days in one year to build BRDF at the DRCS and the Golmud test site, fulfilled the cross-calibration of GF-1/PMS (panchromatic and multispectral sensors) based on MODIS and Landsat-8/OLI data [10]. Chen *et al*. employed the Shuffled Complex Evolution-University of Arizona algorithm for the cross-calibration of the GF-4/VNIR

Manuscript received September 2, 2020; revised November 25, 2020 and December 17, 2020; accepted December 20, 2020. Date of publication December 23, 2020; date of current version January 13, 2021. This work was supported in part by the Science and Technology of Henan province under Grant 202102310015 and Grant 212102310029, in part by the National Natural Science Foundation of China under Grant 41671345, and in part by the Land Observation Satellite Supporting Platform of National Civil Space Infrastructure Project. *(Corresponding author: Zui Tao.)*

Jie Han and Xiaoguo Guan are with the School of Urban and Environment Sciences, Xuchang University, Xuchang 461000, China (e-mail: hanjie@radi.ac.cn; guanguo666@163.com).

Zui Tao and Qiyue Liu are with the Aerospace Information Research Institute, Chinese Academy of Sciences, Beijing 100101, China (e-mail: taozui@radi.ac.cn; liuqy@radi.ac.cn).

Yong Xie is with the School of Geography and Remote Sensing, Nanjing University of Information Science and Technology, Nanjing 210044, China (e-mail: xieyong@nuist.edu.cn).

Huina Li is with the School of Electrical and Mechanical Engineering (Engineering Training Center), Xuchang University, Xuchang 461000, China (e-mail: lihuina851013@163.com).

Digital Object Identifier 10.1109/JSTARS.2020.3046738

sensor with the Landsat-8/OLI sensor [11]. Wang *et al*. discussed the contribution of each uncertainty to the cross-calibration of huanjing-1 (HJ-1)/charge-coupled device (CCD) and provided many valuable references for improving calibration accuracy [12]. Chander *et al*. focused on the influence of the SBAF on cross-calibration accuracy since the relative spectral response (RSR) differences between the reference and calibrated sensors produced different observation results over the same target [13].

Previous studies have shown that only when a well-calibrated sensor has a band setting similar to that of a calibrated sensor, the cross-calibration method can be applied to obtain highly accurate calibration coefficients. However, it is difficult to find an available reference sensor with the same band setting as GF-6/WFV, especially for the four new bands. Consequently, Yang *et al*. only obtained the cross-calibration coefficients of GF-6/WFV in the blue, green, red and NIR bands [5]. Therefore, the best way to optimize the cross-calibration method to obtain all calibration coefficients of GF-6/WFV for all eight bands, even without enough valid reference bands, should be determined to achieve the quantitative applications of this type of sensor. Therefore, taking the MODIS sensor as the reference and the DRCS as the study area, a novel radiometric cross-calibration method for GF-6/WFV is proposed.

The organization of this article is as follows: the WFV and MODIS sensors, the test site and the datasets are described in Section II. Section III introduces the proposed cross-calibration principle of GF-6/WFV. The results of the radiometric cross-calibration and validation are illustrated in Section IV. In Section V, the advantages of the proposed method compared with the traditional cross-calibration method are presented, the consistency of the cross-calibration results using the MODIS and Sentinel-2A/MSI sensors as the references are analyzed, the influences of the interpolation method and the SBAF correction on the cross-calibration accuracy are focused on, and the total calibration uncertainty is calculated. Section VI is a summary and conclusion of the article.

II. Satellites, Test Site, and Datasets

A. Satellites

The GF-6 satellite, a polar orbit satellite associated with the Chinese high-resolution Earth observation system, was launched on June 2, 2018. In addition to four popular bands (blue, green, red and NIR), the WFV on the GF-6 satellite senses four new bands that are crucial for vegetation remote sensing research, including one coastal band (400–450 nm), one yellow band (590–630 nm) and two red-edge bands (690–730 nm and 730–770 nm). The ground sample distance (GSD) and swath of WFV images are 16 m and 800 km, respectively [5], [14]. WFV images are freely downloaded from the CRESDA[1]. Unlike the GF-1/WFV sensor, which uses four WFV cameras to acquire images with an 800-km swath, the GF-6/WFV sensor only uses one camera to meet this demand [5], [9].

MODIS, aboard the polar Terra satellite launched on December 18, 1999, can provide near-daily global coverage data with 36 bands and a 2330-km swath [15]. Although it has operated for more than two decades, the onboard calibration system can make MODIS TOA reflectance products with approximately 2% uncertainty and at-sensor spectral radiance products with approximately 5% uncertainty [16]. Therefore, MODIS sensors are often treated as radiometric reference sensors and used to calibrate sensors without onboard calibration assemblies. MODIS images and related products can be freely downloaded from the level 1 and atmosphere archive and distribution system[2].

In this article, five bands of MODIS products are used to obtain the radiometric calibration coefficients of WFV. The corresponding information of MODIS and WFV are given in Table I. The RSRs of MODIS and WFV are illustrated in Fig. 1.

TABLE I
Information of PMS and MODIS

Sensor	Band Number	Band Type	Spectral Range (nm)	GSD (m)	Swath(km)
WFV	1	Blue	450-520	16	800
	2	Green	520-590		
	3	Red	630-690		
	4	NIR	770-890		
	5	RedEdge1	690-730		
	6	RedEdge2	730-770		
	7	Costal	400-450		
	8	Yellow	590-630		
MODIS	1	Red	620-670	500	2330
	2	NIR	841-876		
	3	Blue	459-479		
	4	Green	545-565		
	5	SWIR	1230-1250		

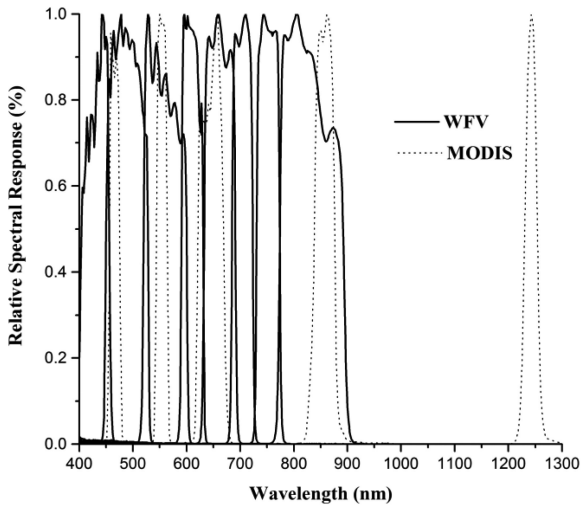

Fig. 1. RSRs of WFV and MODIS.

B. Test Site

With the advantage of a low coefficient of variation (the ratio of standard deviation (SD) and mean reflectance), flat terrain, homogeneous surface, good radiation direction and low aerosol levels, the DRCS, as illustrated in Fig. 2, which has geographic coordinates of 40.04° N-40.28° N and 94.17° E-94.5° E and

[1][Online]. Available: http://www.cresda.com/CN/

[2][Online]. Available: https://earthdata.nasa.gov/eosdis/daacs/laads

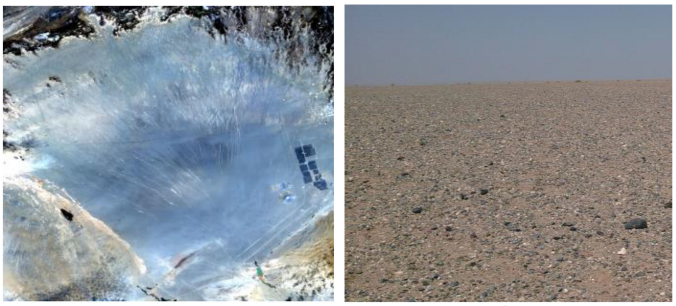

(a) (b)

Fig. 2. Dunhuang test site. (a) GF-6/WFV image. (b) Detailed landscape.

TABLE II
INFORMATION OF CROSS-CALIBRATION IMAGE PAIRS OVER DRCS IN 2019. VZ, VA, SZ, AND SA ARE THE VIEW ZENITH ANGLE, THE VIEW AZIMUTH ANGLE, THE SOLAR ZENITH ANGLE, AND THE SOLAR AZIMUTH ANGLE, RESPECTIVELY

Date	Sensor	Time	VZ(°)	VA(°)	SZ(°)	SA(°)
2019.01.11	MODIS	13:00	34.70	-75.96	63.09	167.34
	WFV	13:00	18.81	302.96	63.14	166.80
2019.07.01	MODIS	12:40	4.57	-81.17	21.66	137.34
	WFV	12:37	30.93	88.38	22.55	134.02
2019.10.21	MODIS	12:40	4.86	-84.19	51.82	166.09
	WFV	13:10	22.42	300.56	50.94	174.52
2019.10.28	MODIS	12:45	15.89	-79.13	53.92	168.72
	WFV	12:42	27.93	88.17	54.20	166.58
2019.11.06	MODIS	12:40	4.67	-82.17	56.99	167.57
	WFV	13:01	7.77	334.38	56.38	172.72

is approximately 1200 m above sea level, is often used to implement cross-calibration and site calibration experiments [17], [18]. The CRESDA implements annual site calibration at this site and publishes the OCCs of land observation satellites, such as GF-1/WFV/PMS, GF-2/PMS, HJ-1/CCD, GF-4/VNIR, and GF-6/WFV/PMS. The DRCS is also treated as a radiometric transfer platform to evaluate radiometric differences between two sensors and monitor the on-orbit radiometric degradation of sensors [4], [10], [18].

C. Datasets

According to the valid data filter criteria for cross-calibration proposed by Xie *et al*. [8], five groups of valid image pairs over the DRCS are collected. The information on these images is given in Table II, which shows that the view angles of the WFV and MODIS images are quite different. Therefore, the BRDF characteristics of the DRCS need to be taken into account in the process of radiometric cross-calibration.

To ensure the same research area and reduce the geometric registration error, the centre of the DRCS (approximately 2500 × 2500 m) is treated as the investigated target, which covers 5 × 5 pixels on the MODIS images with a 500-m GSD and 156 × 156 pixels on the WFV images with a 16-m GSD.

Since the swaths of MODIS and WFV are both large, the solar illuminations (solar zenith and azimuth angles) and view geometries (viewing zenith and azimuth angles) over the investigated target should be accurately extracted. For MODIS, these parameters are extracted from MOD03. For WFV, they are extracted from the angle file (*.nav) in the original data package with the thin plate spline interpolation method.

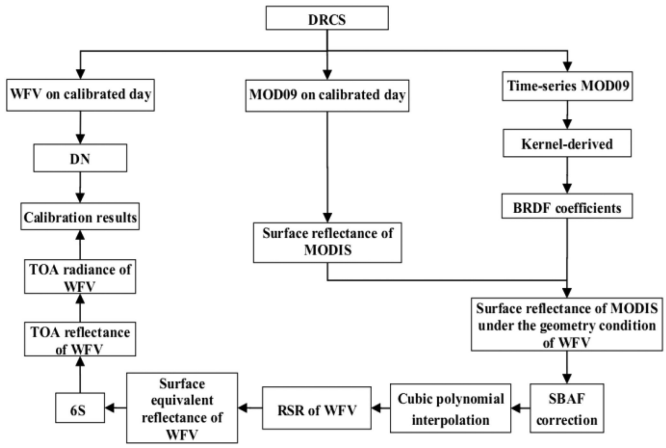

Fig. 3. Flowchart of the experiment.

III. METHODOLOGY

To implement radiometric cross-calibration for GF-6/WFV without the corresponding available reference bands, a novel radiometric cross-calibration method is developed in this article. Fig. 3 shows the flowchart of our experiment.

The novel radiometric cross-calibration of GF-6/WFV with MODIS in the DRCS consists of the following ten steps.

1) The surface reflectance of MOD09 products, $\rho^{\mathrm{M\_Sref}}$, over the investigated target on the calibrated days are extracted.
2) The Ross–Li BRDF model, as shown in (1), is used to obtain the BRDF coefficients [18], [19]

$$\rho(\theta_v,\theta_s,\phi) = f_{iso}(\lambda) + f_{geo}(\lambda)k_{geo}(\theta_v,\theta_s,\phi) + f_{vol}(\lambda)k_{vol}(\theta_v,\theta_s,\phi) \quad (1)$$

where $\rho(\theta_v,\theta_s,\phi)$ is the bidirectional reflectance; θ_v, θ_s , and ϕ are the sensor zenith angle, the solar zenith angle, and the relative azimuth angle, respectively; and f_{iso}, f_{geo}, and f_{vol} are the Lambertian scattering component, the coefficient of the LiSparse-Reciprocal geometric scattering and the RossThick volume scattering, respectively.

Although MCD43A1 production can provide the BRDF coefficients in bands 1–7 of MODIS with a 500-m GSD, all these products over the DRCS on the calibrated days are unavailable. Therefore, after using MOD35 products and the normalized difference snow index to eliminate images contaminated by cloud clusters and snow, respectively, valid time-series MOD09 data (104 scenes) over the DRCS in 2019 are collected. The surface reflectance of the MOD09 products and the corresponding geometric parameters extracted from MOD03 are incorporated into (1) to obtain the BRDF coefficients for five bands with the least square method. Table III gives the BRDF coefficients of the DRCS based on the valid time-series MOD09 data in 2019.

3) According to the geometric parameters of MODIS and WFV and the BRDF coefficients given in Table III, the simulated surface reflectance under the geometric conditions of MODIS, $\rho^{\mathrm{M\_brdf}}$, and that of WFV, $\rho^{\mathrm{W\_brdf}}$,

TABLE III
BRDF COEFFICIENTS OF DRCS BASED ON THE VALID TIME-SERIES MOD09 IN 2019

BRDF Coefficients	Blue	Green	Red	NIR	SWIR
f_{iso}	0.1779	0.2309	0.2673	0.2785	0.3056
f_{vol}	0.0668	0.0951	0.1192	0.1359	0.1373
f_{geo}	0.0166	0.0209	0.0247	0.0236	0.0283

under the geometric conditions of WFV are derived by (1). The BRDF correction coefficient, C, is calculated by using

$$\mathrm{C} = \frac{\rho^{\mathrm{W\_brdf}}}{\rho^{\mathrm{M\_brdf}}}. \tag{2}$$

4) Fig. 1 shows that the RSRs of WFV and MODIS in the blue, green, red, and NIR bands are notably different. Therefore, the RSR differences must be adjusted using the SBAF in this proposed cross-calibration method [13]. The SBAF correction coefficients are calculated by (3). Since the WFV sensor has no shortwave infrared (SWIR) band, the SBAF correction coefficient in the SWIR band is set to 1.0 in this article. The influence of this assumption on the cross-calibration results is discussed in Section V

$$\mathrm{SBAF} = \frac{\rho^{\mathrm{W\_V}}/\rho^{\mathrm{V\_brdf}} * \rho^{\mathrm{W\_brdf}}}{\rho^{\mathrm{M\_V}}/\rho^{\mathrm{V\_brdf}} * \rho^{\mathrm{W\_brdf}}} = \frac{\rho^{\mathrm{W\_V}}}{\rho^{\mathrm{M\_V}}} \tag{3}$$

where $\rho^{\mathrm{V_brdf}}$is the simulated equivalent surface reflectance at the vertical observation angle, calculated by (1). The surface equivalent reflectance of WFV, $\rho^{\mathrm{W\_V}}$, and that of MODIS, $\rho^{\mathrm{M\_V}}$, at the vertical observation angle are derived using the measured averaged surface profile at the vertical observation angle with analytical spectral devices (ASDs) from July 31, 2014, to August 6, 2014 over the DRCS by (4) and (5), respectively,

$$\rho^{\mathrm{W\_V}} = \frac{\int \rho^{\mathrm{ASD}} \times \mathrm{RSR}_{\mathrm{WFV}}(\lambda) d\lambda}{\int \mathrm{RSR}_{\mathrm{WFV}}(\lambda) d\lambda} \tag{4}$$

$$\rho^{\mathrm{M\_V}} = \frac{\int \rho^{\mathrm{ASD}} \times \mathrm{RSR}_{\mathrm{MODIS}}(\lambda) d\lambda}{\int \mathrm{RSR}_{\mathrm{MODIS}}(\lambda) d\lambda} \tag{5}$$

where $\mathrm{RSR}_{\mathrm{WFV}}(\lambda)$ and $\mathrm{RSR}_{\mathrm{MODIS}}(\lambda)$ are the RSRs of WFV and MODIS, respectively, and ρ^{ASD} is the measured averaged surface profile with ASDs over the DRCS.

5) Considering the BRDF correction and SBAF correction, the surface reflectance of MOD09, $\rho^{\mathrm{M\_Sref}}$, in five bands is converted to the surface reflectance under the geometric conditions of WFV, $\rho^{\mathrm{W\_Sref}}$, by

$$\rho^{\mathrm{W\_Sref}} = \mathrm{C} \times \mathrm{SBAF} \times \rho^{\mathrm{M\_Sref}}. \tag{6}$$

6) The cubic polynomial interpolation method is applied to obtain a continuous spectral profile of the DRCS under the geometric conditions of WFV, $\rho^{\mathrm{W\_CSref}}$. Fig. 4 shows that the interpolated continuous surface reflectance under the geometric conditions of WFV over the DRCS on different days has a similar shape as that of the measured averaged surface reflectance.

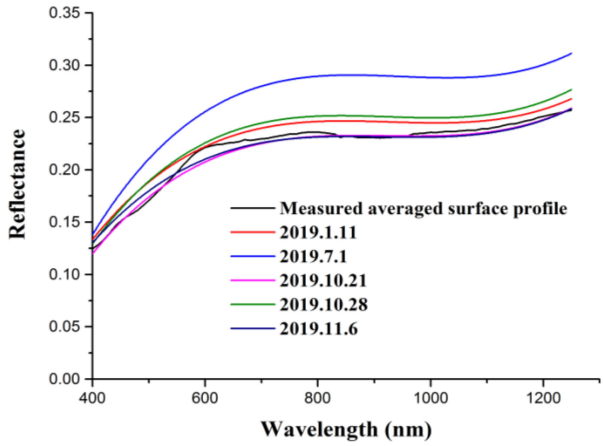

Fig. 4. Measured averaged reflectance and the interpolated continuous surface reflectance of DRCS on different calibrated days.

TABLE IV
MAIN SIMULATIVE PARAMETERS USED IN 6S

Parameters	Value				
	2019.01.11	2019.07.01	2019.10.21	2019.10.28	2019.11.06
Observation Geometry of WFV	Listed in Table II				
Atmospheric Conditions	Midlatitude Winter	Midlatitude Summer	Midlatitude Winter	Midlatitude Winter	Midlatitude Winter
Aerosol Type	Desert				
AOT@550 nm [a]	0.032	0.110	0.054	0.051	0.051
Altitude	1200m				

[a] AOT(aerosol optical thickness) @550 nm is derived from the MOD04_L2 aerosol product.

7) The surface equivalent reflectance of GF-6/WFV, $\rho^{\mathrm{W\_ESref}}$, in eight bands is calculated by

$$\rho^{\mathrm{W\_ESref}} = \frac{\int \rho^{\mathrm{W\_CSref}} \times \mathrm{RSR}_{\mathrm{WFV}}(\lambda) d\lambda}{\int \mathrm{RSR}_{\mathrm{WFV}}(\lambda) d\lambda}. \tag{7}$$

8) The surface equivalent reflectance of WFV in eight bands, $\rho^{\mathrm{W\_ESref}}$, is converted to the simulated TOA reflectance of WFV, $\rho^{\mathrm{W\_Tref\_sim}}$, with the aid of the 6S radiative transfer model and the simulative parameters given in Table IV.

9) The simulated TOA radiance of the WFV images, $L^{\mathrm{W\_Trad\_sim}}$, is calculated as

$$L^{\mathrm{W\_Trad\_sim}} = \frac{\rho^{\mathrm{W\_Tref\_sim}} \times \mathrm{ESUN}^{\mathrm{W}} \times \cos\theta_s^{\mathrm{W}}}{\pi d^2} \tag{8}$$

where $\mathrm{ESUN}^{\mathrm{W}}$ is the TOA solar irradiance of WFV; d is the Earth-Sun distance; and θ_s^{W} is the solar zenith angle of the WFV images.

10) Finally, the calibration coefficient gain of WFV, G^{W}, is calculated by (9). It should be noted that, currently, for the GF series satellite sensor data, the calibration coefficient offset caused by the dark current and other factors has been eliminated (0 for each band), so the

TABLE V
PMCs OF WFV AND THE SDs

Band of WFV	2019.01.11	2019.07.01	2019.10.21	2019.10.28	2019.11.06	SD
1	0.0689	0.0679	0.0694	0.0701	0.0701	0.0009
2	0.0529	0.0521	0.0523	0.0533	0.0531	0.0005
3	0.0505	0.0495	0.0492	0.0508	0.0503	0.0007
4	0.0335	0.0346	0.0336	0.0338	0.0340	0.0004
5	0.0558	0.0511	0.0533	0.0561	0.0574	0.0025
6	0.0485	0.0467	0.0465	0.0480	0.0490	0.0011
7	0.0815	0.0735	0.0780	0.0835	0.0821	0.0040
8	0.0537	0.0540	0.0527	0.0550	0.0536	0.0008

TABLE VI
RELATIVE ERROR BETWEEN THE PMCs AND THE OCCs

Band of WFV	OCCs	Relative Error (%)				
		2019.01.11	2019.07.01	2019.10.21	2019.10.28	2019.11.06
1	0.0705	2.27	3.69	1.56	0.57	0.57
2	0.0567	6.70	8.11	7.76	6.00	6.35
3	0.0516	2.13	4.07	4.65	1.55	2.52
4	0.0322	4.04	7.45	4.35	4.97	5.59
5	0.0532	4.89	3.95	0.19	5.45	7.89
6	0.0453	7.06	3.09	2.65	5.96	8.17
7	0.0786	3.69	6.49	0.76	6.23	4.45
8	0.0585	8.21	7.69	9.91	5.98	8.38

calibration coefficient only includes the gain value [5], [10], [18]

$$G^{\mathrm{W}} = \frac{L^{\mathrm{W\_Trad\_sim}}}{\mathrm{DN}^{\mathrm{W}}} \tag{9}$$

where DN^{W} is the averaged DN of the WFV images over the investigated target.

IV RESULTS

A. Cross-Calibration Results

According to the proposed radiometric cross-calibration method, the proposed method coefficients (PMCs) of WFV on the five calibrated days and the SDs are calculated and given in Table V. The SDs of the eight bands are all less than 0.4%, which shows that the PMCs on different calibrated days have good consistency and indicates that the proposed cross-calibration method is stable.

B. Validation With the OCCs

Although Table V gives that the PMCs derived from the five image pairs on different calibrated days have good consistency, the reliability of the radiometric calibration accuracies of the PMCs needs to be validated.

The OCCs of WFV, published in 2019 by the CRESDA, with the site calibration method are treated as the reference information, which has a sufficiently high accuracy, to validate the cross-calibration accuracy [3], [10], [18], [20]. The relative error between the OCCs and the PMCs is calculated and given in Table VI. The relative error is defined as the absolute value of "PMCs/OCCs-1."

TABLE VII
BRDF CORRECTION COEFFICIENTS BETWEEN WFV AND MODIS

Date	Blue	Green	Red	NIR
2019.01.11	0.9310	0.9586	0.9686	0.9687
2019.07.01	1.0938	1.0629	1.0531	1.0522
2019.10.21	0.9597	0.9626	0.9644	0.9657
2019.10.28	1.1015	1.0749	1.0652	1.0636
2019.11.06	0.9684	0.9745	0.9769	0.9776

TABLE VIII
SBAF CORRECTION COEFFICIENTS BETWEEN WFV AND MODIS

Date	Blue	Green	Red	NIR
2019.01.11	0.9986	1.0097	1.0033	0.9699
2019.07.01	1.0066	1.0057	0.9969	0.9481
2019.10.21	1.0071	1.0097	1.0014	0.9741
2019.10.28	0.9986	1.0099	1.0005	0.9739
2019.11.06	1.0045	1.0097	1.0014	0.9728

It can be seen that the PMCs are close to the OCCs in the eight bands, which indicates that the proposed cross-calibration method is suitable for WFV even with the lack of corresponding available reference bands. It is encouraging that the relative errors between the OCCs and the PMCs are all less than 8.38%, except for that of the yellow band on October 21, 2019.

V. DISCUSSION

A. WFV Calibrated by the Traditional Cross-Calibration Method

The traditional cross-calibration method employs the linear regression between the simulated TOA radiance or reflectance derived from the reference sensor, which has a similar band setting as the calibrated sensor, and the corresponding DN extracted from the calibrated sensor image over the investigated target to calculate the cross-calibration results [3], [9], [21]. In this part, the traditional cross-calibration method is used to obtain cross-calibration coefficients for bands 1–4 of WFV, which have similar band settings as those of MODIS. The main steps of the traditional cross-calibration method, with the MODIS sensor as the reference, are as follows.

1) The TOA reflectance of the MOD02HKM data over the investigated target is extracted.
2) The BRDF coefficients are derived from the TOA reflectance of the time-series MODIS images in 2019 by (1) [10], [18], [22]. Then, the BRDF correction coefficients are calculated by (2) based on the observational geometric information of MODIS and WFV, the corresponding values are given in Table VII.
3) The SBAF correction coefficients for each band are calculated (as given in Table VIII) based on the simulative parameters are given in Table IV [13], [23]. The surface profile is the averaged surface profile measured by the ASDs from July 31, 2014, to August 6, 2014.
4) The TOA reflectance of MODIS is converted to the simulated TOA radiance of WFV based on the BRDF correction coefficients and the SBAF correction coefficients. Finally,

TABLE IX
CROSS-CALIBRATION RESULTS AND THE RELATIVE ERROR USING THE TRADITIONAL CROSS-CALIBRATION METHOD

	Band of WFV	2019.01.11	2019.07.01	2019.10.21	2019.10.28	2019.11.06
Cross-calibration Results	1	0.0681	0.0658	0.0678	0.0702	0.0687
	2	0.0538	0.0517	0.0531	0.0542	0.0534
	3	0.0511	0.0492	0.0494	0.0507	0.0502
	4	0.0331	0.0338	0.0331	0.0333	0.0331
Relative Error (%)	1	3.40	6.67	3.83	0.43	2.55
	2	5.11	8.82	6.35	4.41	5.82
	3	0.97	4.65	4.26	1.74	2.71
	4	2.80	4.97	2.80	3.42	2.80

the cross-calibration coefficients are derived using the traditional cross-calibration method.

The cross-calibration results and the relative errors involved when using the traditional cross-calibration method are given in Table IX. The relative error is defined as the absolute value of "the traditional calibration coefficients/OCCs-1."

It is encouraging that the maximum relative error of the cross-calibration result is reduced from 8.82% for the traditional cross-calibration method to 8.11% for the proposed cross-calibration method. This indicates that the traditional cross-calibration method, which can only obtain the cross-calibration coefficients for similar bands as those of the calibrated sensor, can be replaced by the proposed cross-calibration method to derive cross-calibration results for all eight bands of WFV.

B. Consistency Analysis of Calibration Results Using Different Reference Satellites

In this part, the Sentinel-2A/MSI sensor is treated as a reference sensor to obtain the PMCs. The consistency of the cross-calibration results obtained using different reference satellites is analyzed. The main derived steps of the cross-calibration results using the MSI sensor are as follows.

1) The valid image pairs of WFV and Sentinel-2A/MSI, acquired on July 1, 2019 over the DRCS, are collected. The time interval of the image pairs is 10 min.
2) The TOA reflectance values of the MSI over the investigated target in the blue, green, red, and NIR bands are extracted and converted to surface reflectance values of the MSI with the aid of the 6S radiative transfer model.
3) According to the BRDF coefficients given in Table III and the SBAF correction coefficients derived by (3)–(5), the surface reflectance of MSI under the geometry condition of WFV is derived by (6).
4) The cubic polynomial interpolation method is used to obtain the continuous spectral profile of the DRCS. The surface equivalent reflectance of WFV is derived by (7). Then, the TOA reflectance of WFV is derived with the aid of the 6S radiative transfer model, which is converted to the TOA radiance of WFV by (8).
5) Finally, the calibration coefficients of WFV using the Sentinel-2A/MSI sensor as the reference sensor are calculated by (9).

TABLE X
CROSS-CALIBRATION RESULTS OF WFV BASED ON MODIS AND MSI

Date	Band of WFV	MODIS	MSI	Relative Error (%)
2019.07.01	1	0.0679	0.0659	2.95
	2	0.0521	0.0509	2.30
	3	0.0495	0.0502	1.41
	4	0.0346	0.0351	1.45
	5	0.0511	0.0525	2.74
	6	0.0467	0.0483	3.43
	7	0.0735	0.0728	0.95
	8	0.0540	0.0537	0.56

TABLE XI
RELATIVE ERROR BETWEEN THE OCCS AND THE PMCS AFTER RESET THE SBAF CORRECTION COEFFICIENT IN SWIR BAND

	Band of WFV	Relative Error (%)				
		2019.01.11	2019.07.01	2019.10.21	2019.10.28	2019.11.06
SBAF Increasing by 0.1	1	2.27	3.69	1.56	0.43	0.57
	2	6.70	8.11	7.76	6.00	6.35
	3	2.13	4.26	4.84	1.55	2.71
	4	4.04	7.45	4.35	4.97	5.28
	5	4.70	4.14	0.00	5.26	7.71
	6	7.06	2.87	2.43	5.74	7.95
	7	3.56	6.74	1.02	5.98	4.33
	8	8.21	7.69	9.91	5.98	8.38
SBAF Decreasing by 0.1	1	2.27	3.83	1.56	0.57	0.57
	2	6.88	8.29	7.94	6.00	6.35
	3	1.94	4.07	4.65	1.36	2.52
	4	4.04	7.45	4.35	5.28	5.59
	5	5.08	3.76	0.38	5.64	8.08
	6	7.51	3.31	2.87	6.18	8.39
	7	3.94	6.36	0.64	6.36	4.58
	8	8.21	7.69	9.91	5.98	8.38

Table X gives the cross-calibration results and the relative errors of WFV using MODIS and MSI sensors as reference sensors on the same calibrated day. The relative error is defined as the absolute value of "the cross-calibration coefficient using MSI as a reference/the cross-calibration coefficient using MODIS as a reference – 1." Table X demonstrates that the cross-calibration results obtained using the two reference sensors are in good agreement. The maximum relative error is 3.43%.

C. Influence of SBAF Correction on Calibration Results

In the proposed cross-calibration method, the SBAF correction coefficient in the SWIR band is set to 1.0. Therefore, this part will focus on whether this setting will influence the calibration results. The SBAF correction coefficient in the SWIR band is increased by 0.1 and decreased by 0.1 to recalculate new cross-calibration coefficients [11]. Then, the relative errors between the OCCs and the new cross-calibration coefficients are given in Table XI. Compared with Table VI, the differences in the relative errors are all less than 0.44%, which indicates that the setting of the SBAF correction coefficient in the SWIR band is reasonable.

D. Influence of the Interpolation Method on Calibration Results

In the proposed cross-calibration method, the cubic polynomial interpolation method is employed to obtain the continuous spectral profile of the DRCS. Whether this interpolation method is suitable for interpolating the spectral profile of the DRCS

TABLE XII
RELATIVE ERROR BETWEEN THE OCCS AND THE PMCS USING THE CUBIC SPLINE INTERPOLATION METHOD

Band of WFV	Relative Error (%)				
	2019.01.11	2019.07.01	2019.10.21	2019.10.28	2019.11.06
1	2.55	3.97	1.70	0.57	0.85
2	7.41	8.99	8.29	6.35	7.05
3	1.36	3.10	4.07	1.16	1.74
4	3.73	7.14	4.04	4.97	5.28
5	5.45	3.20	0.75	5.64	8.83
6	7.28	3.31	2.65	5.52	8.61
7	4.96	4.58	0.38	7.12	6.11
8	8.03	7.52	9.91	5.81	8.38

should be discussed. Therefore, in this part, the cubic spline interpolation method is used to replace the cubic polynomial interpolation method.

Compared with Table VI, Table XII gives that most of the relative errors of the PMCs obtained using the cubic spline interpolation method are very close to those obtained using the cubic polynomial interpolation method. The maximum relative errors of the two interpolation methods are also the same. Therefore, the cubic polynomial interpolation method and the cubic spline interpolation method are both suitable for obtaining the continuous spectral profile of the DRCS in the proposed cross-calibration method.

E. Total Uncertainty of the Cross-Calibration

Since not all of the factors can be quantified, the total uncertainty of the final cross-calibration coefficients is estimated here. There are eight main factors of influence in this article.

1) *MOD09*: The root mean square errors (RMSEs)of MOD09 in bands 1–5 of MODIS are obtained according to a previous study [24]. Then, the RMSEs are treated as perturbations that are brought into the surface reflectance of MOD09 over the DRCS to recalculate new cross-calibration coefficients. The maximum relative differences between the new cross-calibration coefficients and the coefficients in Table V for each band on different days are treated as the uncertainty values for MOD09.
2) *Geometric mismatching*: Although the homogeneous spectral regions are treated as the investigated targets, geometric mismatching between the WFV and MODIS images will affect the cross-calibration accuracy. Therefore, the shifted sliding-window method is used [12], [23]. The sliding windows (156×156 pixels) of the WFV image are shifted by 63 pixels (approximately 1000 m). Then, the new averaged DN values extracted from the shifted sliding windows are used to recalculate the new cross-calibration coefficients. The maximum relative differences between the new cross-calibration coefficients and the coefficients in Table V for each band on different days are treated as the uncertainty values for geometric mismatching.
3) *BRDF correction*: In this article, since the surface reflectance of the time-series MOD09 data is selected to obtain the BRDF coefficients with the Kernel-derived model, several factors may contribute to uncertainty in the BRDF correction, such as MOD09, the Kernel-derived model, the solar and view angles, and the stability of the surface reflectance values.

The BRDF coefficients given in Table III are used to obtain the modeled surface reflectance by (1). Then, the RMSEs between the modeled and observed surface reflectance values of the time-series MOD09 data (104 scenes) are treated as the uncertainty values in the kernel-derived model in bands 1–5 of MODIS [19]. The errors of the solar angles are neglected. The observation angles are increased by 0.1° and are then used to calculate the new modeled surface reflectance values of the time-series MOD09 data. The RMSEs between the original and new modeled surface reflectance values are taken as the uncertainty of the observation angles in bands 1–5 of MODIS. The observed surface reflectance values of the time-series MOD09 are converted to the surface reflectance values at a vertical observation angle, of which the SDs are taken as the uncertainty of the stability of the surface reflectance values in bands 1–5 of MODIS. Consequently, the total uncertainty caused by MOD09, the kernel-derived model, the solar and view angles and the stability of surface reflectance in bands 1–5 of MODIS are calculated by the square root method. This total uncertainty is treated as the perturbation that is brought into the derived surface reflectance of the DRCS in bands 1–5 of MODIS. Then, the perturbed derived surface reflectance values of the DRCS in bands 1–5 of MODIS are brought into the cubic polynomial interpolation method to obtain the perturbed interpolated continuous spectral profile of the DRCS, which is used to recalculate new cross-calibration coefficients. The maximum relative differences between the new cross-calibration coefficients and the coefficients given in Table V for each band on different days are treated as the uncertainty values associated with the BRDF correction.

1) Interpolation method: According to the results of the analysis of the influence of the interpolation method on the calibration results, the maximum differences in the relative errors given in Tables VI and XII for each band are treated as the uncertainty values associated with the interpolation method.
2) 6S model: The uncertainty of the cross-calibration result caused by the 6S model is approximately 1.6% [5], [25].
3) AOT value: Since the AOT derived from the MOD04_L2 is used to convert the surface equivalent reflectance of WFV to the TOA radiance of WFV with aid of the 6S radiative transfer model, the accuracy of AOT may affect the cross-calibration uncertainty. The uncertainty of the AOT value derived from the MOD04_L2 aerosol product is approximately $\pm 0.05 \pm 0.15\tau$ [26]. The corresponding cross-calibration uncertainty values associated with the AOT value are given in Table XIII.
4) Aerosol type: Since the DRCS has mixed desert and continental aerosol types, the desert aerosol type given in Table IV may affect the cross-calibration uncertainty [11]. Therefore, the aerosol type is set as the continental aerosol type to recalculate new cross-calibration coefficients. Then, the maximum relative differences between the new cross-calibration coefficients and the coefficients given in Table V for each band on different days are treated

TABLE XIII
TOTAL CALIBRATION UNCERTAINTY

Symbol	Band of WFV							
	1	2	3	4	5	6	7	8
MOD09 (%)	0.73	0.76	0.79	0.30	0.58	0.61	0.54	0.92
Geometric Mismatching (%)	0.89	1.17	1.43	1.17	1.59	1.30	0.68	1.12
BRDF Correction (%)	2.12	2.57	2.88	3.15	2.91	3.00	1.61	2.72
Interpolation Method (%)	0.28	0.88	0.97	0.31	0.94	0.44	1.91	0.17
6S Model (%)	1.60	1.60	1.60	1.60	1.60	1.60	1.60	1.60
AOT@550nm (%)	0.58	0.19	0.60	0.60	0.54	0.63	1.21	0.38
Aerosol Type (%)	1.49	1.76	1.64	2.06	1.79	1.97	0.96	1.69
SBAF Correction (%)	0.14	0.18	0.19	0.31	0.19	0.44	0.25	0.00
Total Uncertainty(%)	3.32	3.88	4.19	4.33	4.28	4.28	3.47	3.88

as the uncertainty values associated with the aerosol type given in Table XIII.

5) SBAF correction: According to the results of the analysis of the influence of the SBAF correction on the calibration results, the maximum differences between the new cross-calibration coefficients, obtained by resetting the SBAF correction coefficient in the SWIR band, and the coefficients in Table V for each band are treated as the uncertainty values for the SBAF correction.

Table XIII gives the uncertainties caused by various factors and the total uncertainty. The total uncertainty calculated by the square root method is less than 4.33%.

VI. CONCLUSION

In this article, a novel on-orbit radiometric cross-calibration approach is proposed to realize the radiometric cross-calibration of GF-6/WFV sensors even without enough available reference bands. The details of this proposed method are described in this article. Taking the DRCS as the radiometric transfer platform and treating MODIS as the reference sensor, the surface reflectance of MOD09 is extracted. The BRDF coefficients of the DRCS are obtained based on the valid time-series MOD09 in 2019, which are applied to correct the bidirectional reflectance effect of the DRCS. The SBAF correction coefficients are used to adjust the RSR differences between the reference sensor and the calibrated sensor. Then, the cubic polynomial interpolation method is employed to obtain the continuous spectral profile of the DRCS from bands 1–5 of MODIS. The surface equivalent reflectance values of GF-6/WFV in the eight bands are calculated by the spectral convolution method with the RSRs of GF-6/WFV. Then, the TOA reflectance values of GF-6/WFV in the eight bands are derived with the aid of the 6S model. Finally, according to the corresponding DN over the DRCS, the calibration coefficients are calculated.

The validation results show that the PMCs on different calibrated days are close to each other, and the SDs are less than 0.4%. Taking the OCCs as the references, the PMCs have good consistency with the OCCs, the relative errors of the PMCs are all less than 8.38% except for that of the yellow band on October 21, 2019. Compared with the traditional cross-calibration method, the maximum relative errors in the blue, green, red, and NIR bands are reduced from 8.82% to 8.11% when using the proposed cross-calibration method, which indicates that the proposed cross-calibration method can not only obtain higher consistency with the OCCs but can also derive the radiometric cross-calibration coefficients of the eight bands even without available reference bands. Additionally, the Sentinel-2A/MSI sensor is used to assess the consistency of the radiometric cross-calibration results using different reference satellites. The results show that the PMCs obtained using MODIS and MSI sensors as references also have good consistency.

The influences of the SBAF correction and the interpolation method on the calibration results are discussed. It is found that the different interpolation methods and the SBAF correction coefficient setting in the SWIR band have a slight influence on the calibration results. Moreover, the total uncertainty of our proposed method associated with MOD09, geometric mismatching, the BRDF correction, the interpolation method, the 6S model, the AOT value, the aerosol type, and the SBAF correction is less than 4.33%.

In the future, we will discuss whether using the interpolation method to obtain a continuous TOA spectral profile with which to derive radiometric cross-calibration coefficients can improve the overall radiometric cross-calibration accuracy of GF-6/WFV, which will further optimize the calibration scheme and improve the on-orbit radiometric calibration accuracy of this type of sensor.

ACKNOWLEDGMENT

The authors would like to thank the CRESDA (http://www.cresda.com/CN/) for providing GF-6 satellite imagery. The MODIS data were downloaded from the Level 1 and Atmosphere Archive and Distribution System (https://earthdata.nasa.gov/about/daacs/daac-laads). The Sentinel-2A/2B MSI data were downloaded from the Copernicus Open Access Hub (https://scihub.copernicus.eu/dhus/#/home). The authors would also like to thank the anonymous reviewers.

REFERENCES

[1] K. J. Thome, "Absolute radiometric calibration of Landsat 7 ETM+ using the reflectance-based method," *Remote Sens. Environ.*, vol. 78, no. 1-2, pp. 27–38, Oct. 2001.

[2] G. Chander, B. L. Markham, and D. L. Helder, "Summary of current radiometric calibration coefficients for Landsat MSS, TM, ETM+, and EO-1 ALI sensors," *Remote Sens. Environ.*, vol. 113, no. 5, pp. 893–903, May 2009.

[3] H. Gao, X. Gu, T. Yu, Y. Sun, and Q. Liu, "Cross-calibration of GF-1 PMS sensor with Landsat 8 OLI and Terra MODIS," *IEEE Trans. Geosci. Remote Sens.*, vol. 54, no. 8, pp. 4847–4854, Aug. 2016.

[4] C. Gao *et al.*, "Radiometric cross-calibration of GF-4/VNIR sensor with Landsat8/OLI, Sentinel-2/MSI, and Terra/MODIS for monitoring its degradation," *IEEE J. Sel. Top. Appl. Earth Observ. Remote Sens.*, vol. 13, pp. 2337–2350, May 2020.

[5] A. Yang *et al.*, "Radiometric cross-calibration of the wide field view camera onboard Gaofen-6 in multispectral bands," *Remote Sens.*, vol. 12, no. 6, Mar. 2020, Art. no. 1037.

[6] C. Gao *et al.*, "An investigation of a novel cross-calibration method of FY-3C/VIRR against NPP/VIIRS in the Dunhuang test site," *Remote Sens.*, vol. 8, no. 1, Jan. 2016, Art. no. 77.

[7] J. Li, L. Feng, X. Pang, W. Gong, and X. Zhao, "Radiometric cross calibration of Gaofen-1 WFV cameras using Landsat-8 OLI images: A simple image-based method," *Remote Sens.*, vol. 8, no. 5, May 2016, Art. no. 411.

[8] Y. Xie, J. Han, X. Gu, and Q. Liu, "On-orbit radiometric calibration for a space-borne multi-camera mosaic imaging sensor," *Remote Sens.*, vol. 9, no. 12, Dec. 2017, Art. no. 1248.
[9] L. Feng, J. Li, W. Gong, X. Zhao, X. Chen, and X. Pang, "Radiometric cross-calibration of Gaofen-1 WFV cameras using Landsat-8 OLI images: A solution for large view angle associated problems," *Remote Sens. Environ.*, vol. 174, pp. 56–68, Mar. 2016.
[10] Q. Liu, T. Yu, and H. Gao, "Radiometric cross-calibration of GF-1 PMS sensor with a new BRDF model," *Remote Sens.*, vol. 11, no. 6, Mar. 2019, Art. no. 707.
[11] Y. Chen, K. Sun, D. Li, T. Bai, and C. Huang, "Radiometric cross-calibration of GF-4 PMS sensor based on assimilation of Landsat-8 OLI images," *Remote Sens.*, vol. 9, no. 8, Aug. 2017, Art. no. 811.
[12] Z. Wang *et al.*, "Uncertainty analysis of cross-calibration for HJ-1 CCD camera," *Sci. China*, vol. 56, no. 3, pp. 713–723, Mar. 2013.
[13] G. Chander *et al.*, "Applications of spectral band adjustment factors (SBAF) for cross-calibration," *IEEE Trans. Geosci. Remote Sens.*, vol. 51, no. 3, pp. 1267–1281, Mar. 2013.
[14] M. Wang *et al.*, "On-orbit geometric calibration and accuracy verification of GF-6 WFV camera," *Acta Geodaeticaet Cartographica Sinica*, vol. 49, no. 2, pp. 171–180, Feb. 2020.
[15] A. Angal, X. Xiong, and A. Shrestha. "Cross-calibration of MODIS reflective solar bands with Sentinel 2A/2B MSI instruments," *IEEE Trans. Geosci. Remote Sens.*, vol. 58, no. 7, pp. 5000–5007, Jul. 2020.
[16] X. Xiong *et al.*, "Multiyear on-orbit calibration and performance of Terra MODIS reflective solar bands," *IEEE Trans. Geosci. Remote Sens.*, vol. 45, no. 4, pp. 879–889, Apr. 2007.
[17] X. Hu *et al.*, "Characterization of CRCS Dunhuang test site and vicarious calibration utilization for Fengyun (FY) series sensors," *Can. J. Remote Sens.*, vol. 36, no. 5, pp. 566–582, 2010.
[18] L. Liu *et al.*, "Satellite-based time series calibration of GF-1 WFV sensors for large view zenith angle observations." *Int. J. Remote Sens.*, vol. 39, no. 22, pp. 8293–8316, Jul. 2018.
[19] W. Lucht, C. B. Schaaf, and A. H. Strahler, "An algorithm for the retrieval of albedo from space using semiempirical BRDF models," *IEEE Trans. Geosci. Remote Sens.*, vol. 38, no. 2, pp. 977–998, Mar. 2000.
[20] Y. Zhao, L. Ma, C. Li, C. Gao, N. Wang, and L. Tang, "Radiometric cross-calibration of Landsat-8/OLI and GF-1/PMS sensors using an instrumented sand site," *IEEE J. Sel. Top. Appl. Earth Observ. Remote Sens.*, vol. 11, no. 10, pp. 3822–3892, Oct. 2018.
[21] H. Gao, D. Jupp, Y. Qin, X. Gu, and T. Yu, "Cross-calibration of the HSI sensor reflective solar bands using hyperion data," *IEEE Trans. Geosci. Remote Sens.*, vol. 53, no. 7, pp. 4127–4137, Feb. 2015.
[22] J. Han, Z. Tao, Y. Xie, Q. Liu, and Y. Huang, "Radiometric cross-calibration of GF-4/PMS based on radiometric block adjustment," *IEEE Trans. Geosci. Remote Sens.*, to be published, doi: 10.1109/TGRS.2020.3009740.
[23] G. Chander, D. L. Helder, D. Aaron, N. Mishra, and A. K. Shrestha, "Assessment of spectral, misregistration, and spatial uncertainties inherent in the cross-calibration study," *IEEE Trans. Geosci. Remote Sens.*, vol. 51, no. 13, pp. 1282–1296, Mar. 2013.
[24] M. Broomhall, H. Chedzey, B. MeAtee, P. Fearns, and M. Lynch, "Validation of the extended suite of MOD09 and SMAC-processed reflectance products for Australian terrestrial supersites: A case study," *AGU Fall Meeting*, 2014.
[25] E. F. Vermote, D. Tanre, J. L. Deuze, M. Herman, and J.-J. Morcette, "Second simulation of the satellite signal in the solar spectrum, 6S: An overview," *IEEE Trans. Geosci. Remote Sens.*, vol. 35, no. 3, pp. 675–686, May 1997.
[26] L. A. Remer *et al.*, "The MODIS aerosol algorithm, products, and validation," *J. Atmos. Sci.*, vol. 62, no. 4, pp. 947–973, Apr. 2005.

Jie Han received the B.S. and M.S. degrees in science and technology of surveying and mapping from the Henan Polytechnic University, Jiaozuo, China, in 2009 and 2012, respectively, and the Ph.D. degree in geography and geographic information system from the Institute of Remote Sensing and Digital Earth, Chinese Academy of Sciences, Beijing, China, in 2015.

He is currently a Lecturer with the School of Urban and Environment Sciences, Xuchang University, Xuchang, China. He has worked on the radiomimetic and geometric processing of remote sensing images. His main research interest include quantitative remote sensing applications in the visible/near-infrared.

Zui Tao was born in China in 1984. He received the B.S. degree from Henan University, Kaifeng, China, in 2005, the M.S. degree from Wuhan University, Wuhan, China, in 2008, and the Ph.D. degree from the Institute of Remote Sensing and Digital Earth, Chinese Academy of Sciences (CAS), Beijing, China, in 2012, all in cartography and geographic information system.

He is currently a Research Assistant with Aerospace Information Research Institute, CAS. His research interests include validation of remote sensing product, ecological, and environmental remote sensing.

Yong Xie received the B.S. and M.S. degrees in physics from the Nanjing Normal University, Nanjing, China, in 2000 and 2004, respectively, and Ph.D. degree in earth science and geoinformation system from George Mason University, Fairfax, VA, USA, in 2009.

He is currently a Professor with the School of Geographical Science, Nanjing University of Information Science and Technology, Nanjing, China. He has worked on the radiomimetic calibration and characterization of satellite remote sensor and science product validation with ground measurements.

Huina Li received the B.S. and M.S. degrees in electronic information engineering and communication and information system from the Henan Polytechnic University, Jiaozuo, China, in 2009 and 2012, respectively.

She is currently an Assistant with the School of Electrical and Mechanical Engineering (Engineering Training Center), Xuchang University, Xuchang, China. Her main research interest includes remote sensing image processing in the visible/near-infrared.

Qiyue Liu received the B.S. degree in geographic information system from Hengyang Normal University, Hengyang, China, in 2008 and the M.S. degree in cartography and geography information system from Henan Polytechnic University, Jiaozuo, China, in 2011, and the Ph.D. degree in signal and information processing from the Aerospace Information Research Institute, Chinese Academy of Sciences, Beijing, China, in 2020.

From 2011 to 2014, he was a Probationer with the Institute of Remote Sensing and Digital Earth, Chinese Academy of Sciences, Beijing, China. Since 2014, he has been a Research Assistant. His research interests include radiometric calibration and the validation of remote sensing products.

Xiaoguo Guan received the B.S. degree in science and technology of surveying and mapping from University of Information Engineering, Zhengzhou, China, in 2010 and the M.S. degree in geodesy and surveying engineering from China University of Mining and Technology, Beijing, China, in 2013, and the Ph.D. degree in surveying and mapping engineering from University of Information Engineering, Zhengzhou, China, in 2020.

She is currently an Assistant with the School of Urban and Environment Sciences, Xuchang University, Xuchang, China. Her research interests include remote sensing image processing and BDS/GNSS precision positioning data processing.